Article

The Suppression of Modular Multi-Level Converter Circulation Based on the PIR Virtual Impedance Strategy

Chun Wang [ID], Wenxu Yan *, Wenyuan Wang, Hongyu Ni and Jie Chu

School of Internet of Things, Jiangnan University, Wuxi 214000, China
* Correspondence: ywx01@jiangnan.edu.cn

Abstract: In recent years, with the rise of the electric vehicle industry, there has been significant research on charging and power supply vehicle technologies for electric vehicles. In terms of the corresponding converter usage, modular multi-level converters (MMCs) are also increasingly used in the field of electric vehicle power supply research because of their unique advantages. However, the circulating current problem of MMCs has not been effectively addressed in existing domestic and international studies. In this paper, we propose a proportional-integral resonant (PIR) control method combined with virtual impedance for the optimal suppression of the MMC internal circulating current problem based on the comparison and generalization of the existing methods. Based on the analysis of the working principle of MMCs, this paper proposes and adopts the control strategy of combining virtual impedance and proportional-integral resonance to suppress the circulating current and builds a simulation model in MATLAB to verify that the control strategy proposed in this paper is feasible.

Keywords: MMC; harmonic suppression; circuit circulation; PIR control; virtual impedance; MATLAB/Simulink simulation

1. Introduction

In recent years, with the promotion of new energy use, more and more fields are using new energy as energy supplies. Because of its unique characteristics of new technology, the electric vehicle has many links to new energy storage-related fields for its charging and discharging. The charging and discharging process of an EV battery is inseparable from the converter, and there have been many power electronics pieces of research on the interaction between EVs, power supplies, and grids. Modular multi-level converters (MMCs) have received significant attention since they were proposed in 2002 and have been widely used in power electronic transformers, energy routers, and the energy internet due to their easy scalability, modularity, and applicability to large-capacity applications. Due to their special cascade topology, they have a smoother output waveform and lower switching losses with good application prospects in the field of power converters for electric vehicles [1–3].

In the use of electric vehicle power systems, modular multi-level converters have numerous advantages over conventional converter topologies. MMC circuits are modularly cascaded, have strong scalability, and meet the requirements of various voltage-level applications by cascading different numbers of submodules in the MMC. The MMC avoids the series connection between quantitative power-switching devices, which greatly reduces the converter manufacturing difficulty of the converter [4]. However, the MMC topology also has certain drawbacks compared to the conventional converter. Because of the unbalanced energy distribution between phases, MCCs could cause the formation of circulating currents inside the structure, resulting in more considerable losses inside the converter due to the bridge arm current distortion. It was found that, on the one hand, the presence of circulating harmonics increases the bridge arm current distortion rate, boosts the rated current capacity of the switching components, and increases the system cost; on the other hand, the circulating current increases system losses, leads to higher battery cell temperatures, and accelerates battery aging [5–7].

In the current use and research of MMC devices in various countries, many scholars have studied the internal circulating current of MMCs. From the perspective of passive hardware improvement, some scholars have proposed the method of improving the hardware circuit by increasing the bridge arm reactor to suppress the circulating current, but this increases the overall volume of the MMC, increasing the cost; the system would generate uncontrollable energy internally [8,9]. From the perspective of active control, some scholars have used the traditional proportional-integral (PI) control to achieve the active suppression of the circulating current, controlling the sum of the upper and lower bridge arm voltages as the direct flow without even harmonics, thus eliminating the even harmonics in the circulating current. However, the classical PI controller has limited control gain for AC signals and thus is only suitable for tracking DC signals and cannot completely eliminate a series of even harmonic components in the circulating current [10]. Some scholars have compensated the oscillations of the arm capacitor voltage by compensating the modulation with calculations, but this method requires additional energy to control the loop to achieve system balance [11,12].

This paper proposes a suppression strategy based on MMC harmonic circulation by combining PIR and virtual impedance for the typical MMC system. First, this paper analyzes the topological structure and working principle of MMCs from the objective analysis of suppressing harmonic circulation. Then, we propose a strategy combining virtual impedance and proportional-integral resonance control circulation suppression strategy based on the mathematical analysis of calculating MMC harmonic circulation. Finally, we built a typical MMC circuit simulation model to verify the effectiveness of the strategy of even-harmonic reduction.

2. MMC Analysis

In order to suppress the circulating harmonic current inside the MMC circuit, this section first models and analyzes the MMC circuit. This chapter explains the operation principle of MMCs in the three-phase balanced state and calculates and analyzes the main internal variables of the internal circulating current.

2.1. MMC Model

2.1.1. MMC Basic Circuit

As shown in Figure 1, a typical three-phase MMC circuit topology consists of a three-phase, six-bridge arm with an n submodule SM, a bridge arm reactor L_m, and bridge arm resistance R_m. The three-phase bridge arm on the DC side of the system is jointly connected to the HVDC DC bus, where U_{dc} and I_{dc}, are the current DC bus voltage and current, respectively. The AC side of the system includes equivalent AC reactance L_s and equivalent resistance R_s. The AC side load could be a resistance load, power grid, or a high-voltage motor [13–15].

When the MMC circuit operates in the inverter state, the multi-level voltage waveform is synthesized on the MMC AC side by controlling the input and cutting out of each submodule in the bridge arm, thus emitting active and reactive power to the AC side. The public DC bus of the MMC would also charge and discharge the DC capacitor of the submodule to maintain the stability of the module capacitance-voltage. In Figure 1, u_{uj} and u_{lj} are the module port voltage of the upper and lower bridge arms of the phase. j, i_{uj}, and i_{lj} are the current flowing through the upper and lower bridge arms of the phase. j and U_{sj} are the AC side voltage and the number of phases is $j = a, b, c$.
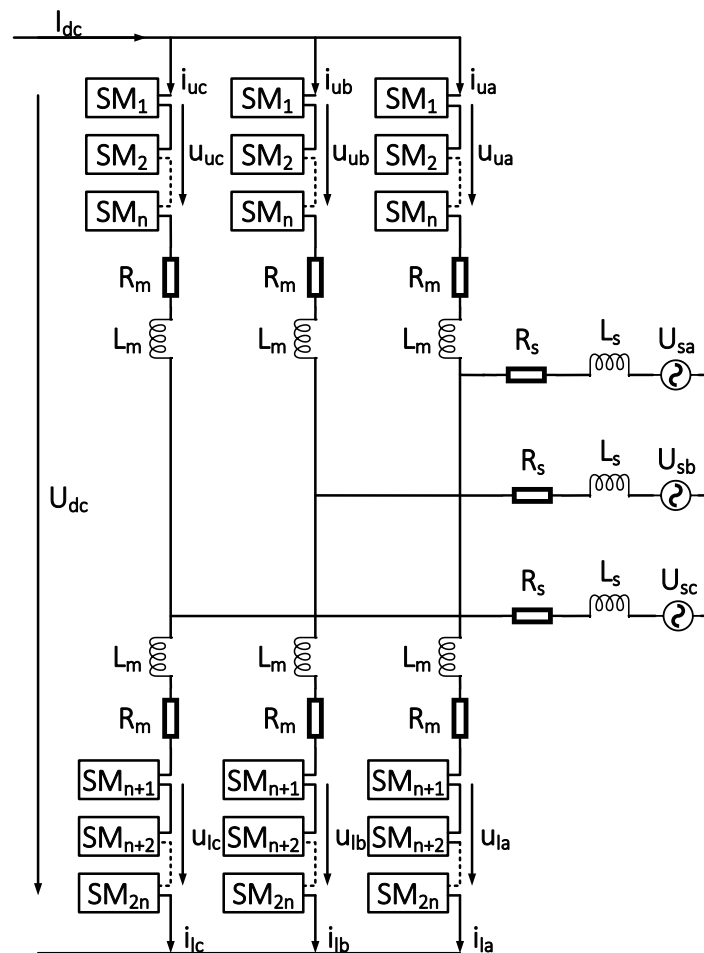
Figure 1. Typical MMC circuit structure.

Under the normal operation of an MMC, the total number of the connecting modules of the upper and lower bridge arm is to ensure the stable voltage of the DC side. The amplitude and the waveform of the output voltage could be changed by changing the difference between the number of input submodules in the upper and lower bridge arms.

Each *SM* in the circuit is an independent submodule, and the MMC submodule has two kinds of half-bridge structures and full-bridge structures [16]. Among them, the half-bridge structure submodule is more widely used due to the small number of devices and better economy. The commonly used MMC half-bridge submodule topology is shown in Figure 2, consisting of two power-switching tubes with anti-parallel diodes and a capacitor.
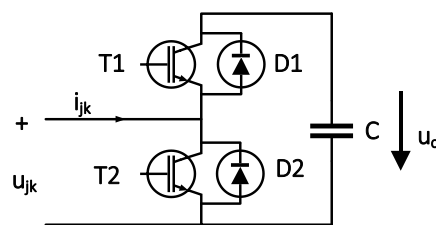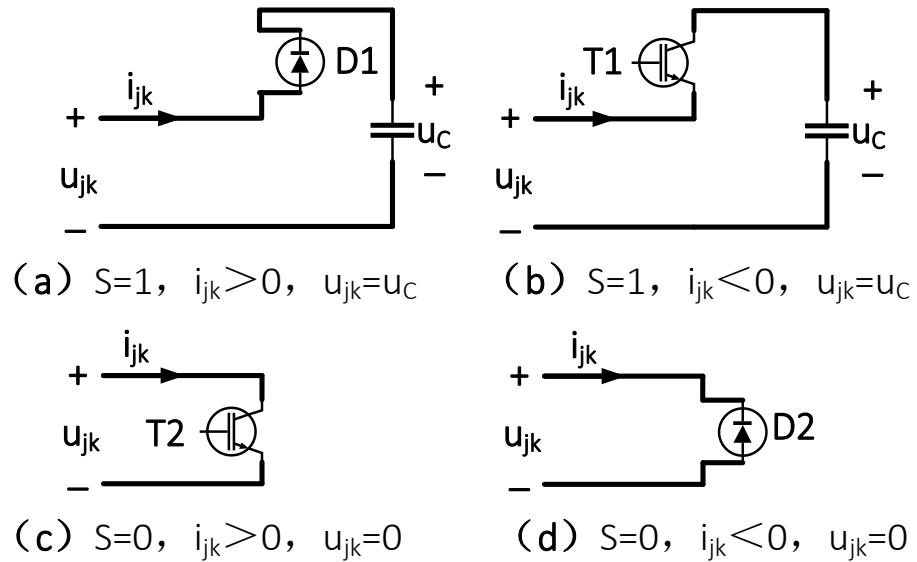

Figure 2. MMC half-bridge submodule structure.

During normal operation, the driving signals of the two power-switch tubes are opposite to avoid a short circuit of the capacitance. The bridge arm flow direction is the internal positive direction of the current i_{jk}, and the working state of the submodule $T1$ is S. According to the power-switch tube drive signal and the corresponding current flow direction, there are four modes of flow channels inside the submodule, as shown in Figure 3.

(1)   When the drive signal of the upper switch T_1 is placed on the submodule, T_1 is in the input state $S = 1$. When the bridge arm current i_{jk} is positive, the current charges the capacitor through the anti-parallel diode $D1$ on the switch $T1$, the capacitance-voltage u_C rises, and the output voltage u_{jk} of the submodule is equal to the capacitance-voltage u_C, as shown in Figure 3a. When the bridge arm current i_{jk} is negative, the current discharges the capacitance through the upper switch tube $T1$, then the capacitance-voltage u_C drops and the output voltage u_{jk} of the submodule is equal to the capacitance-voltage u_C, as shown in Figure 3b.

(2)   When the drive signal of the switch $T1$ is set to 0, the submodule $T1$ is in the bypass state $S = 0$. When the bridge arm current i_{jk} is positive, the current bypasses the capacitance through $T2$, the capacitance-voltage u_C remains unchanged, and the output voltage u_{jk} of the submodule is 0, as shown in Figure 3c. When the bridge arm current i_{jk} is negative, the current bypasses the capacitance through $D2$, and then the capacitance-voltage u_C remains unchanged, and the output voltage u_{jk} of the submodule is 0, as shown in Figure 3d.

（a）S=1，i$_{jk}$>0，u$_{jk}$=u$_C$ （b）S=1，i$_{jk}$<0，u$_{jk}$=u$_C$

（c）S=0，i$_{jk}$>0，u$_{jk}$=0   （d）S=0，i$_{jk}$<0，u$_{jk}$=0

Figure 3. Working principle of an MMC half-bridge submodule. (**a**) Working condition in S = 1, i$_{jk}$ > 0. (**b**) Working condition in S = 1, i$_{jk}$ < 0. (**c**) Working condition in S = 0, i$_{jk}$ > 0. (**d**) Working condition in S = 0, i$_{jk}$ < 0.

Therefore, the relationship between the submodule output voltage and the internal capacitance-voltage of the submodule could be expressed as:

$$u_{jk} = S \times u_C \tag{1}$$

2.1.2. MMC Equivalent Circuit

For the above typical MMC circuit, the following basic assumptions are stated to simplify the analysis:

(1) The system is in a symmetrical three-phase normal operation state; (2) the AC current on the network side is divided symmetrically and evenly between the upper and lower bridge arms; (3) ignore the fluctuation of the DC bus voltage U_{dc}.

Based on the above assumptions, the upper and lower arm voltage of each phase could be equivalent to the AC voltage source u_{uj}, u_{lj}, and the upper and lower arm current could be represented by i_{uj}, i_{lj}, as shown in Figure 4. Then, we built a three-phase equivalent circuit model of a typical MMC topology and performed an internal voltage and current analysis [17–19].
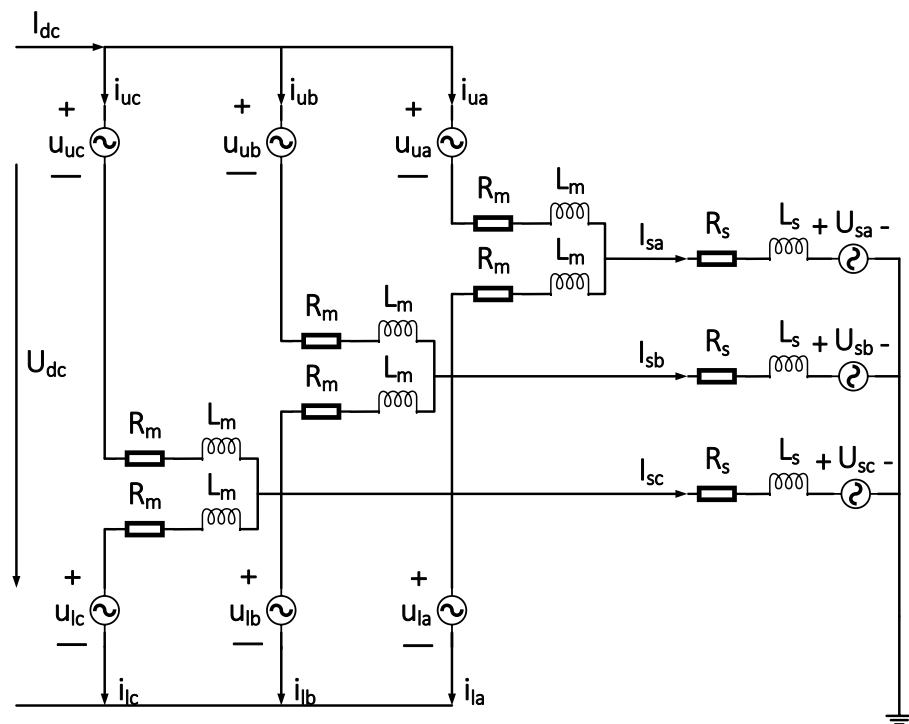
Figure 4. MMC three-phase equivalent model.

Without considering the bridge arm current harmonic component, the three-phase MMC equivalent circuit model is obtained with Kirchhoff's theorem, and the current of the upper and lower bridge arm in each phase is, respectively:

$$\begin{cases} i_{uj} = \frac{I_{dc}}{3} + \frac{I_{sj}}{2} \\ i_{lj} = \frac{I_{dc}}{3} - \frac{I_{sj}}{2} \end{cases} \tag{2}$$

In the equation, I_{dc} is the current in the DC bus, and I_{sj} is the phase current on the network side. Suppose that the number of submodules of the upper and lower bridge arm input conduction is i, j, and since the voltage needs to be kept stable on the DC side, generally:

$$i + j = n. \tag{3}$$

Assume that each submodule has uniform voltage distribution, then the sum of the output voltage of the upper and lower bridge arm submodules u_{uj}, u_{lj} is, respectively:

$$\begin{cases} u_{uj} = \sum_{i=1}^{n} u_{jk} \\ u_{lj} = \sum_{j=1}^{n} u_{jk} \end{cases} \tag{4}$$

In the equation, u_{jk} is the output AC voltage of the upper and lower bridge arm submodule port.

From the MMC equivalent circuit of Figure 4, the upper and lower bridge arms could be regarded in parallel from the AC side, so the characteristic equation of the external characteristics is:

$$U_{sj} = \frac{(u_{uj} - u_{lj})}{2} + (R_s + \frac{R_m}{2})I_{sj} + (L_s + \frac{L_m}{2})\frac{dI_{sj}}{dt} \tag{5}$$

2.2. Circulation Analysis

According to the above analysis, the capacitor of each submodule is evenly divided and balanced at all times, and each capacitance voltage is $U_{dc}/(i+j)$ in the ideal working state. However, in the actual working conditions, the capacitance parameter in each submodule cannot be completely consistent, and the small error of the switch pipe conduction time would lead to the charge and discharge time of each input submodule not being fully synchronized; the capacitance-voltage in each submodule would produce a small deviation, and cannot always be fully balanced. The capacitance-voltage imbalance in the phase bridge arm submodule and the switching is not a completely ideal device and would cause the MMC to produce an alternating harmonic circulation inside [20–22].

Define U_{acj} as the j phase of the AC side's voltage, and the MMC output voltage modulation ratio is m. In practical engineering uses, $m \in (0,1)$ is generally selected:

$$m = \frac{2U_{acj}}{U_{dc}} \tag{6}$$

The power P_{uj}, P_{lj} of each phase's upper and lower bridge arm could be calculated as:

$$\begin{cases} P_{uj} = u_{uj}i_{uj} = \frac{1}{2}U_{dc}[1 - m\sin(\omega t)]\left[\frac{1}{3}I_{dc} + \frac{1}{2}I_{sj}\sin(\omega t + \varphi)\right] \\ P_{lj} = u_{lj}i_{lj} = \frac{1}{2}U_{dc}[1 + m\sin(\omega t)]\left[\frac{1}{3}I_{dc} - \frac{1}{2}I_{sj}\sin(\omega t + \varphi)\right] \end{cases} \tag{7}$$

after calculating, the formula is expanded to obtain the following results:

$$\begin{cases} P_{uj} = \frac{1}{6}U_{dc}I_{dc} - \frac{1}{8}mU_{dc}I_{sj}\cos\varphi - \frac{1}{6}U_{dc}I_{dc}m\sin(\omega t) \\ \qquad + \frac{1}{4}U_{dc}I_{sj}\sin(\omega t + \varphi) + \frac{1}{8}mU_{dc}I_{sj}\cos(2\omega t + \varphi) \\ P_{lj} = \frac{1}{6}I_{dc}U_{dc} - \frac{1}{8}mU_{dc}I_{sj}\cos\varphi + \frac{1}{6}U_{dc}I_{dc}m\sin(\omega t) \\ \qquad - \frac{1}{4}U_{dc}I_{sj}\sin(\omega t + \varphi) + \frac{1}{8}mU_{dc}I_{sj}\cos(2\omega t + \varphi) \end{cases} \tag{8}$$

It could be seen that the power flowing through the upper and lower bridge arms includes the DC component, base frequency, and double frequency components. The external output power of the phase j unit P_{out} and the circulation power inside the ring P_{in} are, respectively:

$$\begin{cases} P_{out} = P_{uj} - P_{lj} = -\frac{1}{3}U_{dc}I_{dc}m\sin(\omega t) + \frac{1}{2}U_{dc}I_{sj}\sin(\omega t) \\ P_{in} = P_{uj} + P_{lj} = \frac{1}{3}U_{dc}I_{dc} - \frac{1}{4}mU_{dc}I_{sj}\cos\varphi + \frac{1}{4}mU_{dc}I_{sj}\cos(2\omega t + \varphi) \end{cases} \tag{9}$$

It could be analyzed that the output power of the MMC to the AC network's side only contains the base wave components; without the DC and harmonic components, the internal circulation power contains a double frequency component. By dividing the circulation power by the voltage, we see that the internal circulation has a second-order harmonic component.

Through the above derivation process, it could be concluded that the MMC bridge arm circulation and the capacitor voltage in the submodule affect each other, the second-order harmonic component of the voltage in each phase cause second-order harmonic circulation, and the second-order circulation further leads to the third-order capacitor's voltage fluctuations in the submodule, and further causes forth-order circulation, which produces messy harmonic components in the MMC. Since the odd harmonics of the upper and lower bridge arms could always cancel each other, only the even harmonic components flow internally. They have opposite symbols, and the phase difference is 120° and in the negative order.

Define the harmonic component of the circulating current present in the bridge arm of phase j as i_{cirj}, so Equation (2) could be modified and rewritten as:

$$\begin{cases} i_{uj} = \frac{I_{dc}}{3} + \frac{I_{sj}}{2} + i_{cirj} \\ i_{lj} = \frac{I_{dc}}{3} - \frac{I_{sj}}{2} + i_{cirj} \end{cases} \tag{10}$$

By defining i_{zj} as the circulation current on the bridge arm and adding i_{uj}, i_{lj} in Equation (10) to offset the AC side I_{sj}, we obtain i_{zj} as:

$$i_{zj} = \frac{i_{uj} + i_{lj}}{2}. \tag{11}$$

According to Equation (10), i_{zj} is composed of direct flow and harmonic superposition so that it could be written as:

$$i_{zj} = \frac{I_{dc}}{3} + i_{cirj} \tag{12}$$

2.3. Modulation Method

In this paper, the nearest level modulation (NLM) was used to perform the submodule modulation of the MMC circuit [23,24]. The nearest level modulation approximates the modulating waveform steps and renders the output waveform produced by the converter similar to the modulating waveform by controlling the input and cut-out of each submodule in the circuit by superimposing the voltage of each submodule. The number of input submodules for the upper and lower bridge arms is as follows:

$$\begin{cases} i = \frac{n}{2} - \text{round}\left[\frac{n}{2} m \sin(\omega t)\right] \\ j = \frac{n}{2} + \text{round}\left[\frac{n}{2} m \sin(\omega t)\right] \end{cases}. \tag{13}$$

where $round[f(x)]$ is the integer function of approximation and the integer with the smallest absolute value of the difference with $f(x)$ is obtained.

3. MMC Circulation Control Strategy

This chapter introduces the MMC circuit harmonic loop suppressor designed in this paper, the principles of the main components of the controller, and the structure of the overall controller.

3.1. Controller Analysis

3.1.1. PIR Control

According to the previous introduction and analysis of the internal working principle of an MMC, it could be learned that the second and fourth-order harmonics are the most important components of the circulating harmonic current, and the high-order current is triggered by the low-order current. Therefore, by reducing the size of the secondary and fourth harmonics, the circulation of each harmonic in the circuit could be effectively suppressed.

The proportional-integral (PI) controller part could realize the unstated difference tracking of the DC components in the circulation, but the AC signal cannot be tracked without the unstated difference. The proportional resonance (PR) controller part could achieve infinite gain at the selected frequency so that it could control a certain frequency, but it needs tedious coordinate transformation and decoupling work before the control process. The proportional-integrated resonance (PIR) controller in the composite current controller could improve the harmonic characteristics and eliminate the derived specific harmonic components so that the controller could achieve a better control effect [25,26].

The traditional PR controller is developed from the internal mode principle, and the general transfer function of the resonant frequency ω_0 is:

$$G_{PR}(s) = K_p + \frac{K_i s}{s^2 + \omega_0^2}. \tag{14}$$

The ideal PR controller could have an infinite gain at the resonant frequency, but there is no gain on either side of this frequency. If the power grid frequency offset occurs, it would directly affect the stability of the system and seriously affect the effect of the controller.

An optimized quasi-proportional-integral resonant controller is proposed in order to maintain the advantages of the PR controller in terms of its high gain while effectively reducing the effects of grid frequency shifts. For the suppression of MMC circulation in this paper, the controller takes second and forth-order frequencies as the main control objects, so the PIR controller transmission function is:
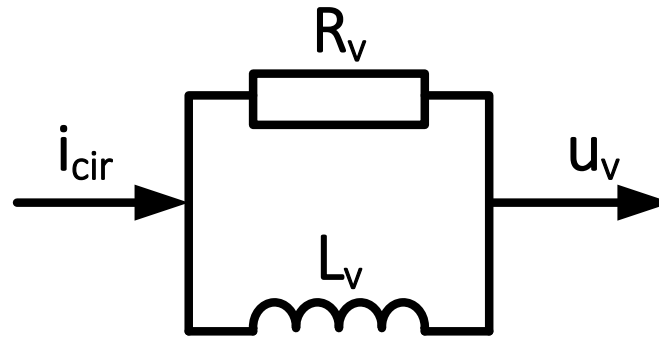
$$G_{PIR}(s) = K_p + \frac{K_i}{s} + \frac{K_{r1}s}{s^2 + \omega_c s + (2\omega_0)^2} + \frac{K_{r2}s}{s^2 + \omega_c s + (4\omega_0)^2} \tag{15}$$

where K_p is the proportional coefficient, K_i is the integral coefficient, K_{r2} and K_{r4} are the resonance control gain of the binary and quadruple frequency, respectively, ω_0 is the base wave frequency, and ω_c is the resonant bandwidth parameter, which controls the range of the resonant frequency (bandwidth), and has the general value 5–15 rad/s.

3.1.2. Virtual Impedance

On the basis of the PIR controller, the additional virtual bridge arm impedance link could effectively undertake the circulation high-order harmonic component suppression function so as to achieve better results. The method of virtual impedance could inhibit many high harmonics with less content in the circulation so that not only the virtual impedance has a small partial pressure on the system, but it also could effectively inhibit the circulation [27,28].

As shown in Figure 5, L_v and R_v constitute the virtual impedance part together, with input i_{cir} as the bridge arm harmonic circulation and output u_v as the correction component of the modulated wave.

Figure 5. Virtual impedance equivalence diagram.

In the controller, the virtual impedance link is the first-order inertial link, whose transfer function is:

$$G_{vir}(s) = \frac{R_v L_v s}{L_v s + R_v} \tag{16}$$

3.2. Controller Instruction

Based on the synthesis of the two controllers, this paper proposed that, based on the PIR virtual impedance control strategy, the control logic is as follows: the bridge arm circulation i_{zj} is through the PIR controller adjustment control modulation wave component u_{pir}, then the harmonic component in the circulation goes through the virtual impedance first-order inertia correction u_{vir}, combining the two together to obtain the modulation wave voltage of the harmonic circulation suppression controller u_h. The overall control block diagram is shown in Figure 6:
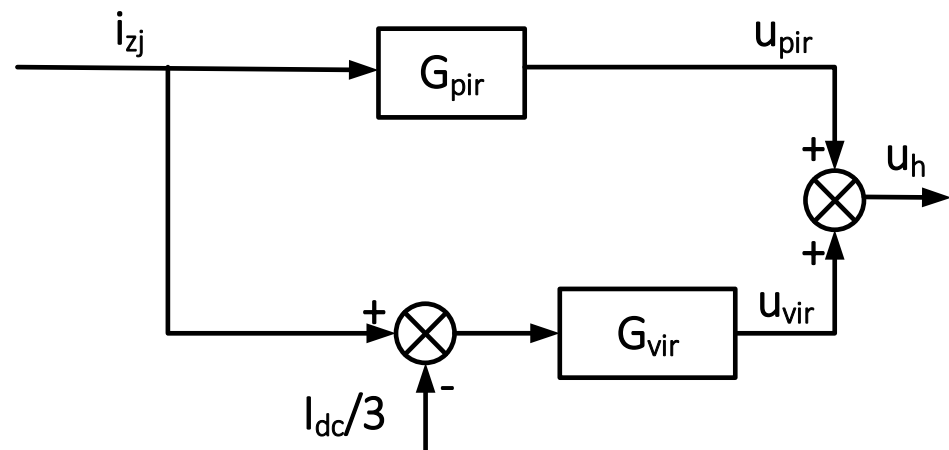
Figure 6. Structural diagram of the PIR virtual impedance controller.

4. Simulation Analysis

In order to verify the effect of the PIR virtual impedance composite control method proposed in this paper, the corresponding model was built in MATLAB for simulation verification (Supplementary Materials: Simulation files S1).

4.1. Simulation Parameters

In this paper, the simulation platform selected the MATLAB2020a Simulink environment and built a three-phase 22 submodule MMC circuit. The circuit adopted the double closed-loop control of the outer loop power control and the inner loop current control; the modulation method adopted the nearest level modulation (NLM) technology. The selected simulation parameters are shown in Table 1, and the selected controller parameters are shown in Table 2 [29,30].

Table 1. Simulation parameters.

Simulation Variable	Parameter Setting
DC bus voltage/kV	5.5
Number of single bridges Arm submodules n	22
Submodule capacitance/mF	7
Bridge arm reaction/mH	8
Switching frequency/kHz	10
Modulation ratio	0.9
Load resistance/Ω	1

Table 2. Controller parameters.

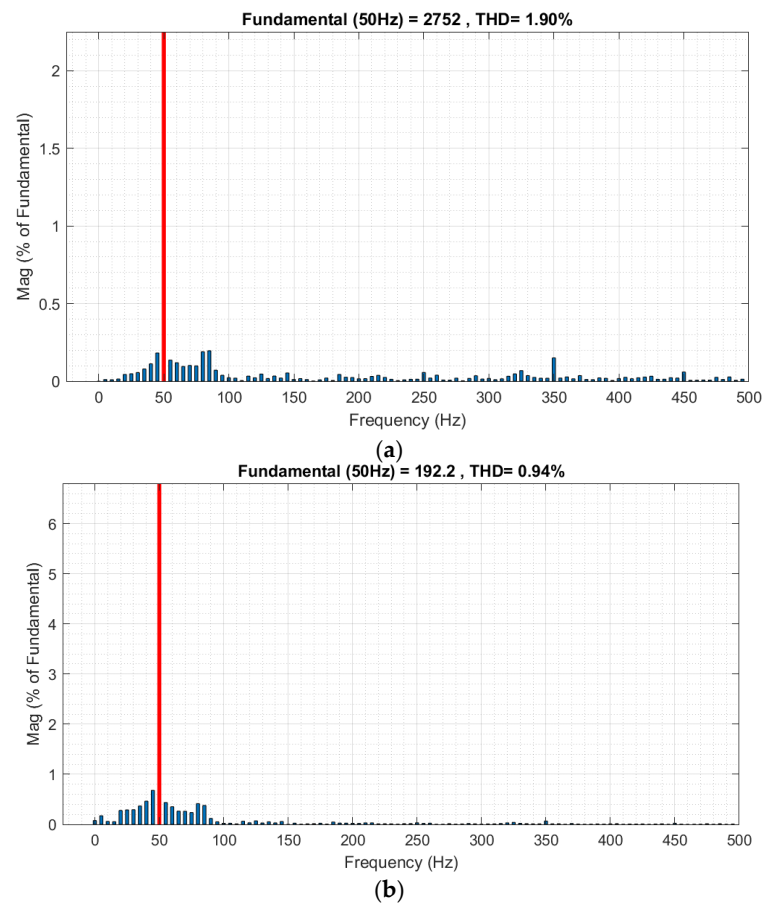| Controller Parameters	Values
K_p	40
K_i	600
K_{r1}	1000
K_{r2}	1000
ω_c	5
R_v/Ω	1
L_v/mH	10

4.2. Simulation Result

4.2.1. Output for the Steady-State Operation

To verify the feasibility of the control strategy used in this paper, the main output quantities in the circuit could be observed so that the steady-state operation control effect of the overall MMC circuit could be observed [31]. The simulation was set to start from t = 0 s, and the active power disturbance was added on the AC side at t = 0.15 s during the simulation to verify the robustness of the circuit against the power fluctuation in the grid-connected operation. The three-phase voltages and currents are shown in their respective pictures using red, blue, and orange.

The voltage and current waveforms of the three-phase AC side output are, respectively, shown in Figure 7a,b. It was observed that before t = 0.15 s, the voltage and current were running in balance; after t = 0.15 s, the voltage and current were also running in balance; at the moment of t = 0.15 s, due to the increase in power, the current automatically increased in order to ensure constant output voltage. The fast Fourier transform (FFT) analysis result shows that the total harmonic distortion (THD) of the three-phase output voltage and current were 1.9% and 0.94%, respectively, as shown in Figure 8a,b. It was observed that the output waveforms worked well with low distortion rates and exhibited good robustness when experiencing power disturbances.
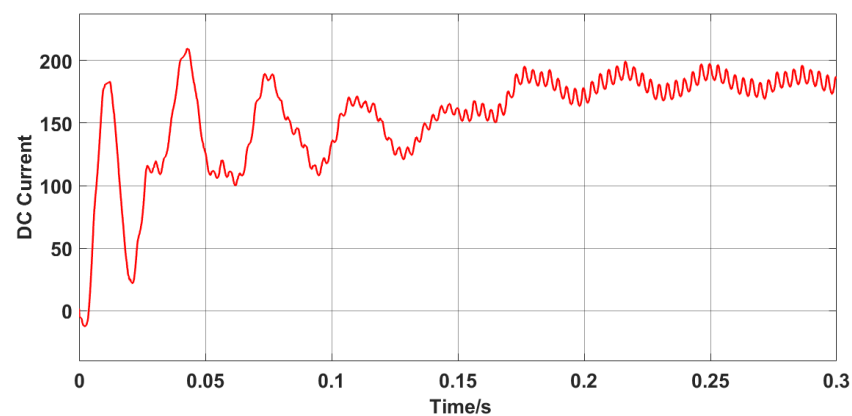

(a)

(b)

Figure 7. (**a**) Three−phase output voltage. (**b**) Three−phase output current.

Fundamental (50Hz) = 2752 , THD= 1.90%

(a)

Fundamental (50Hz) = 192.2 , THD= 0.94%

(b)

Figure 8. (**a**) FFT analysis of the three−phase output voltage. (**b**) FFT analysis of the three−phase output current.

The DC side's current is shown in Figure 9. When the DC side's current reached the steady state, it was controlled to fluctuate within a small range, which was allowed with the normal operating conditions.

Figure 9. DC side's current.

The modulation process is shown in Figure 10, which shows the modulation waves of the upper and lower bridge arms of phase a. It was observed as a step wave similar to the sine waveform with a high degree of symmetry.
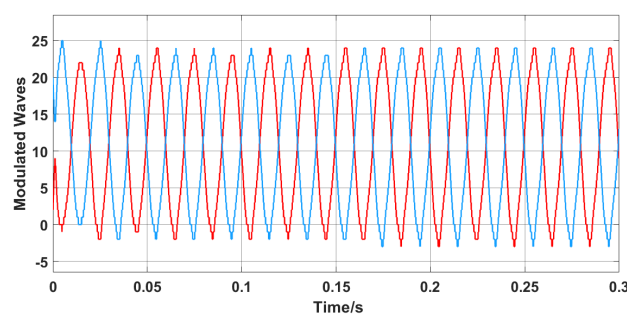
Figure 10. Modulated waves.

According to the analysis above, it is seen that the MMC circuit works stably with good output waveform, and the system has certain robustness under the use of the controller in this paper.

4.2.2. Comparison of the Control Effects

In order to verify the effectiveness of the harmonic circulating current suppression of the MMC circuit in this paper, the effect of the circulating current suppression was compared with that of the open-loop strategy, conventional PI control strategy, and QPR control strategy. The waveform and amplitude of the harmonic loop current component of the MMC circuit during steady-state operation could be observed. The current of the upper bridge arm of phase a was selected as the reference object, and the total harmonic distortion under different control methods was compared with FFT analysis.

The controller, without adding the circulating current suppressor, is shown in Figure 11. The current waveform of the harmonic current component is shown in Figure 11a, and the THD of the arm current was 30.04%, as shown in Figure 11b.
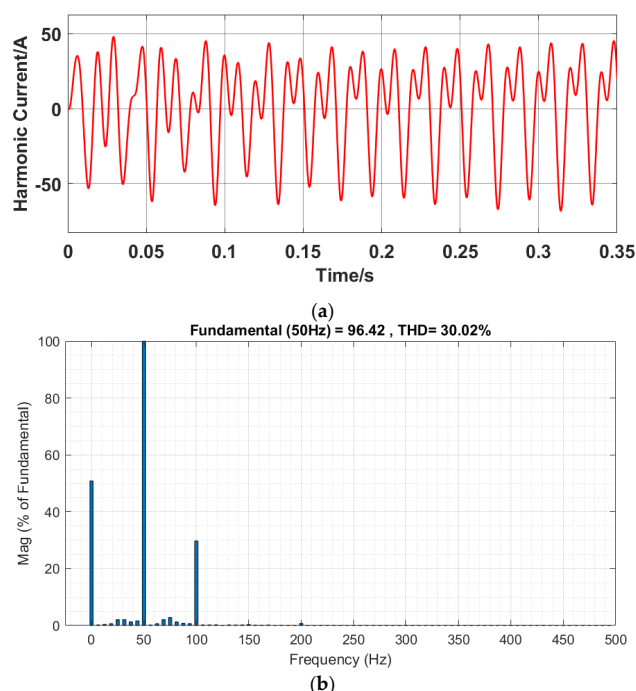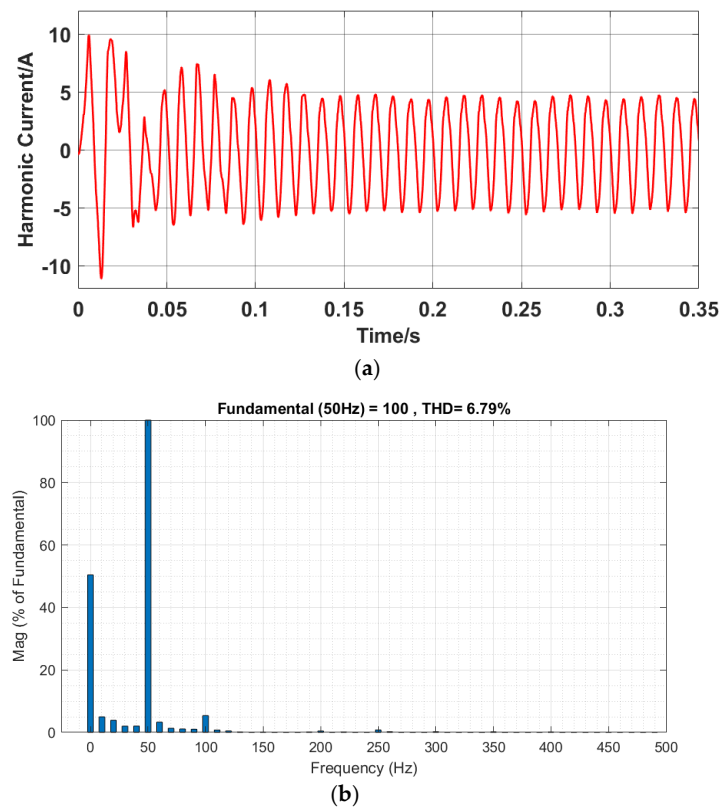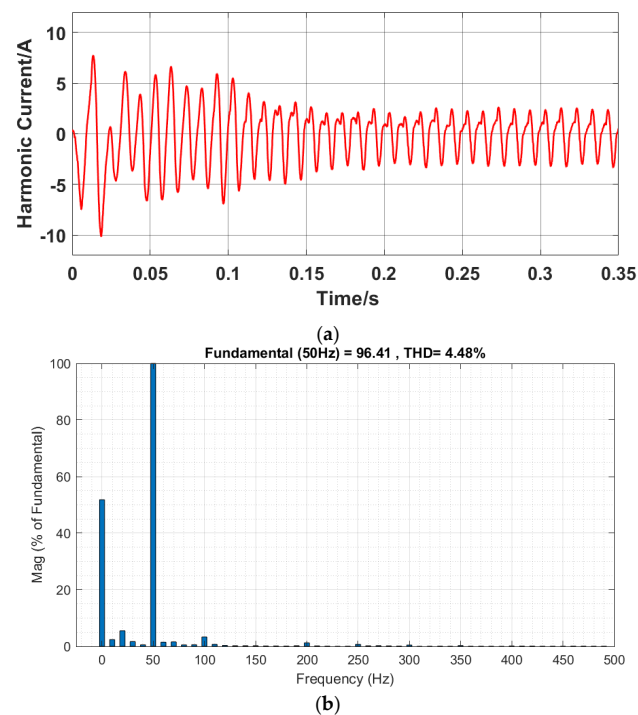

(**a**)

(**b**)

Figure 11. (**a**) Harmonic current without the suppressor. (**b**) FFT analysis of the bridge arm current without the suppressor.

The case of using the PI control circulating current suppressor is shown in Figure 12. The harmonic current component waveform is shown in Figure 12a, and the THD of the arm current was 5.23%, as shown in Figure 12b.
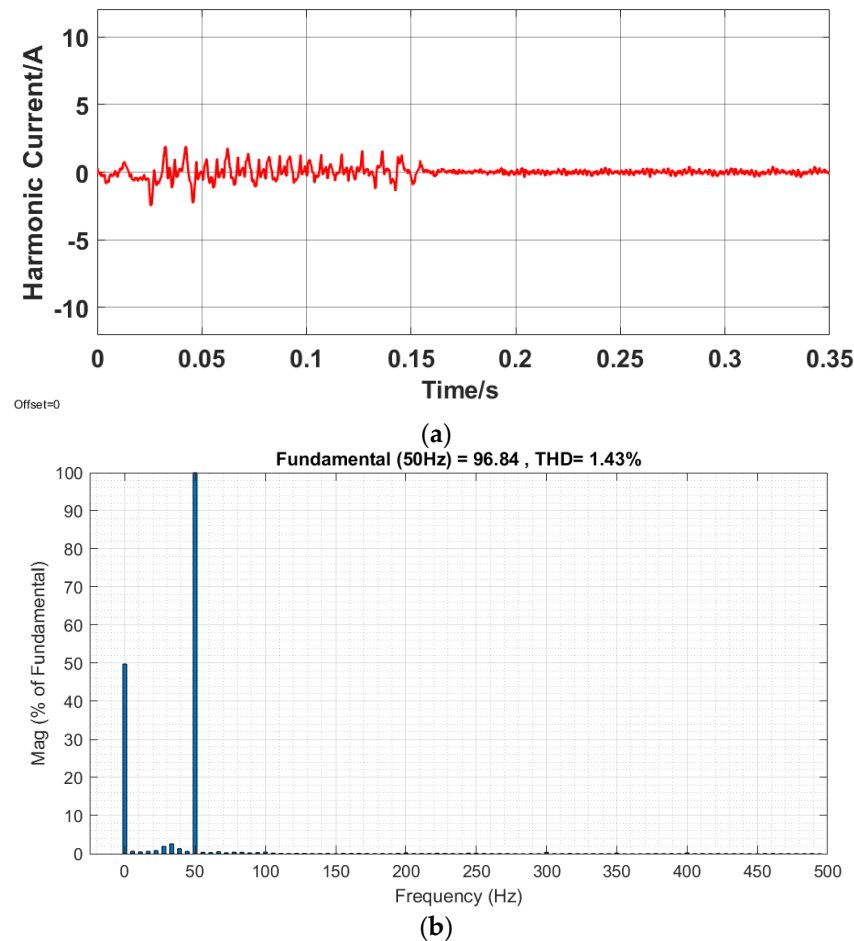
Figure 12. (**a**) Harmonic current with the PI control suppressor. (**b**) FFT analysis of the bridge arm current with the PI control suppressor.

The case of using the QPR control circulating current suppressor is shown in Figure 13. The harmonic current component waveform is shown in Figure 13a, and the THD of the arm current was 4.48%, as shown in Figure 13b.

Figure 13. (**a**) Harmonic current with the QPR control suppressor. (**b**) FFT analysis of the bridge arm current with the QPR control suppressor.

The case of using the PIR virtual impedance composite suppressor designed in this paper is shown in Figure 14. The upper bridge arm current waveform is shown in Figure 14a, and the THD of the arm current was 1.68%, as shown in Figure 14b.

(**a**)

(**b**)

Figure 14. (**a**) Harmonic current with the PIR virtual impedance composite suppressor. (**b**) FFT analysis of the bridge arm current with the PIR virtual impedance composite suppressor.

Table 3 displays the cross-sectional comparisons of the THD of the bridge arm current for the different control methods.

Table 3. Comparisons of the THD using different methods.

Controller Use	THD of the Bridge Arm Current (%)
Without adding the current suppressor	30.02
PI control suppressor	6.79
QPR control suppressor	4.48
PIR virtual impedance composite suppressor	1.43

It is seen from the comparison that the current distortion rate of the bridge arm is very high without adding the circulation control, and there is still a large THD with the addition of the PI circulation control or QPR circulation control. When controlled by the PIR virtual impedance composite harmonic circulating current strategy proposed in this paper, the obtained harmonic current waveform flattens, and the distortion rate is lower, which proves a good control effect.

5. Discussion

With the control strategy used in this paper, the harmonic loops in the circuit could be effectively suppressed, which could reduce component losses in the circuit and extend the component's life. In the field of electric vehicles, this move could lead to optimized output voltage and current, more efficient application of charging lines, and better power quality.

In addition to the work already conducted in this paper, there is still some incompleteness, and these could be considered as subsequent research directions. Since there is no well-built physical experimental platform in this lab, experimental verification has not yet been completed, which would be a long-term work direction to follow. The control strategy proposed in this paper is mainly based on a three-phase balanced circuit, but the operation mode and fault ride-through capability of the circuit under unbalanced conditions were not thoroughly studied.

6. Conclusions

In this manuscript, the internal variables of the MMC circuit were analyzed and explained in detail based on the analysis of its topology in the second chapter. Through circuit derivation, its equivalent circuit was provided, the composition of the internal circulating current was further analyzed, and its harmonic components were explained. In the third chapter of this paper, based on the controller principle, this paper proposed a control method based on the combination of a proportional-integral resonant controller and virtual impedance, which was used to effectively suppress the internal harmonic circulations during the operation of the circuit. In the fourth chapter, the proposed control method was fully simulated through the MATLAB simulation platform. On the one hand, the stability of the operation was analyzed, and it was observed that the three-phase output voltage and current were better, with distortion rates of 1.9% and 0.94%, respectively, and still maintained good robustness when the rated active power fluctuated. On the other hand, the effect of the controller was verified by comparing it with some common circulating current control strategies. The a-phase upper bridge arm current distortion rate was 30.02%, 6.79%, and 4.48% under the traditional open-loop controller, PI controller and QPR controller, respectively, and the distortion rate was 1.43% when the selected controller was used. In summary, it could be concluded that the controller proposed in this paper could effectively suppress the internal harmonic loop current with good results while ensuring the overall stable operation of the circuit.

References

1. Gan, C.; Sun, Q.; Wu, J.; Kong, W.; Shi, C.; Hu, Y. MMC-Based SRM Drives With Decentralized Battery Energy Storage System for Hybrid Electric Vehicles. *IEEE Trans. Power Electron.* **2018**, *34*, 2608–2621. [CrossRef]
2. Guidi, G.; D'Arco, S.; Nishikawa, K.; Suul, J.A. Load Balancing of a Modular Multilevel Grid-Interface Converter for Transformer-Less Large-Scale Wireless Electric Vehicle Charging Infrastructure. *IEEE J. Emerg. Sel. Top. Power Electron.* **2020**, *9*, 4587–4605. [CrossRef]
3. Mao, M.; Ding, Y.; Chang, L.; Hatziargyriou, N.D.; Chen, Q.; Tao, T.; Li, Y. Multi-Objective Power Management for EV Fleet With MMC-Based Integration Into Smart Grid. *IEEE Trans. Smart Grid* **2017**, *10*, 1428–1439. [CrossRef]
4. Wang, D.; Liu, J.; Piegari, L.; Song, S.; Chen, X.; De Simone, D. A Battery Lifetime Improved Control Strategy of Modular Multilevel Converter for Electric Vehicle Application. In Proceedings of the 2019 IEEE 10th International Symposium on Power Electronics for Distributed Generation Systems (PEDG), Xi'an, China, 3–6 June 2019; pp. 594–598. [CrossRef]
5. Gumrukcu, E.; Asadollahi, E.; Joglekar, C.; Ponci, F.; Monti, A.; Guidi, G.; D'Arco, S.; Suul, J.A. Optimal Management for Megawatt Level Electric Vehicle Charging Stations With a Grid Interface Based on Modular Multilevel Converter. *IEEE Access* **2021**, *10*, 258–270. [CrossRef]
6. Wang, W.V.; Thirmawithana, D.J.; Riar, B.; Zane, R. A Novel Integrated Boost Modular Multilevel Converter for High Power Wireless EV Charging. In Proceedings of the 2018 IEEE Energy Conversion Congress and Exposition (ECCE), Portland, OR, USA, 23–27 September 2018; pp. 81–88.
7. Steinsland, V.; Kristensen, L.M.; Arghandeh, R.; Zhang, S. Design of Modular Multilevel Converters for the Shipnet in Medium Voltage DC All-Electric Ships. In Proceedings of the 2020 IEEE 21st Workshop on Control and Modeling for Power Electronics (COMPEL), Aalborg, Denmark, 9–12 November 2020; pp. 1–8.
8. Far, A.J.; Jovcic, D. Small-Signal Dynamic DQ Model of Modular Multilevel Converter for System Studies. *IEEE Trans. Power Deliv.* **2015**, *31*, 191–199. [CrossRef]
9. Bergna, G.; Suul, J.A.; D'Arco, S. State-space modelling of modular multilevel converters for constant variables in steady-state. In Proceedings of the IEEE Workshop Control Modeling for Power Electronics, Trondheim, Norway, 27–30 June 2016; pp. 1–9.
10. Belayneh, N.B.; Park, C.H.; Kim, J.M. Compensation of Arm Current Sensor Errors in Modular Multilevel Converter. *IEEE Trans. Ind. Appl.* **2019**, *55*, 5005–5012. [CrossRef]
11. Sharifabadi, K.; Harnefors, L.; Nee, H.; Norrga, S.; Teodorescu, R. *Design, Control, and Application of Modular Multilevel Converters for HVDC Transmission Systems (series Wiley-IEEE)*; Wiley: Hoboken, NJ, USA, 2016.
12. Prieto-Araujo, E.; Gross, D.; Dörfler, F.; Gomis-Bellmunt, O. Optimal Multivariable MMC Energy-Based Control for DC Voltage Regulation in HVDC Applications. In Proceedings of the 2020 IEEE Power & Energy Society General Meeting (PESGM), Montreal, QC, Canada, 2–6 August 2020; p. 1.
13. Li, H.; Fan, X.; Liu, S. Small-Signal Stability Modeling for MMC-Based DC Grids With Voltage Slope Control and Influence Analysis of Parameters. *IEEE Access* **2021**, *10*, 4686–4698. [CrossRef]
14. Wang, W.; Hang, L.; Qiu, J.; Lu, H.; Zeng, P. Application of MMC based on state observer in DC integration of renewable energy. In Proceedings of the 8th Renewable Power Generation Conference (RPG 2019), Shanghai, China, 24–25 October 2019; pp. 1–6.
15. Bahrani, B.; Debnath, S.; Saeedifard, M. Circulating Current Suppression of the Modular Multilevel Converter in a Double-Frequency Rotating Reference Frame. *IEEE Trans. Power Electron.* **2016**, *31*, 783–792. [CrossRef]
16. Yang, S.; Wang, H.; Chen, H.; Song, W.; Wang, T. Probability-Based Modeling and Analysis for PS-PWM in an MMC Distributed Control System With Sub-Module Asynchrony. *IEEE Trans. Power Electron.* **2019**, *34*, 10392–10397. [CrossRef]
17. Cheng, T.; Zhong, J.; Yang, B.; Wei, Y.; Xu, J.; Zhang, Z. Improved Circulation Suppression Strategy for MMC Considering Low Frequency Oscillation. In Proceedings of the 2021 11th International Conference on Power and Energy Systems (ICPES), China, Shanghai, 18–20 December 2021; pp. 57–61.
18. Bhesaniya, M.M.; Shukla, A. Norton Equivalent Modeling of Current Source MMC and Its Use for Dynamic Studies of Back-to-Back Converter System. *IEEE Trans. Power Deliv.* **2016**, *32*, 1935–1945. [CrossRef]
19. Gao, S.; Ye, H.; Liu, Y. Accurate and Efficient Estimation of Short-Circuit Current for MTDC Grids Considering MMC Control. *IEEE Trans. Power Deliv.* **2019**, *35*, 1541–1552. [CrossRef]
20. Liu, Z.; Zhao, J. Disturbance Interaction Analysis and Suppression Strategy of MMC-HVDC Systems Considering Sub-Module Capacitor Voltage Ripples. *IEEE Trans. Power Syst.* **2020**, *36*, 235–247. [CrossRef]
21. Ji, H.; Chen, A.; Liu, Q.; Zhang, C. A new circulating current suppressing control strategy for modular multilevel converters. In Proceedings of the 2017 36th Chinese Control Conference (CCC), Dalian, China, 26–28 July 2017; pp. 9151–9156.
22. Jia, G.; Chen, M.; Tang, S.; Zhang, C.; Zhao, B. A Modular Multilevel Converter With Active Power Filter for Submodule Capacitor Voltage Ripples and Power Losses Reduction. *IEEE Trans. Power Electron.* **2020**, *35*, 11401–11417. [CrossRef]
23. Qu, L.P.; Lu, Z.; Liu, C.J.; He, C.L. A Sort Method of Balancing Capacitor Voltage of MMC. In Proceedings of the 2019 18th International Symposium on Distributed Computing and Applications for Business Engineering and Science (DCABES), Wuhan, China, 8–10 November 2019; pp. 241–244.
24. Jin, Y.; Wang, S.; Xiao, Q.; Liu, Y.; Mu, Y.; Ji, Y.; Chaudhary, S.K.; Teodorescu, R. A Novel Harmonic Control Method for MMC Combining Improved Nearest Level Control and Selective Harmonic Elimination method. In Proceedings of the 2019 IEEE Energy Conversion Congress and Exposition (ECCE), Baltimore, MD, USA, 29 September–3 October 2019; pp. 6368–6375.

25. Zuo, Y.; Zhu, J.; Yuan, X.; Lee, C.H.T. Two-degree-of-freedom Quasi-PIR Controller for Smooth Speed Control of Permanent Magnet Vernier Machine. In Proceedings of the 2021 IEEE Energy Conversion Congress and Exposition (ECCE), Vancouver, BC, Canada, 10–14 October 2021; pp. 5022–5028.
26. Jun, S.; Zhen, X. An Improved Control Strategy for Double Feed Induction Generator in Low Frequency Resonant Power Grid. In Proceedings of the 2018 37th Chinese Control Conference (CCC), Wuhan, China, 25–27 July 2018; pp. 7460–7464.
27. Wai, R.J.; Zhang, Q.Q.; Wang, Y. A Novel Voltage Stabilization and Power Sharing Control Method Based on Virtual Complex Impedance for an Off-Grid Microgrid. *IEEE Trans. Power Electron.* **2019**, *34*, 1863–1880. [CrossRef]
28. Micallef, A.; Apap, M.; Spiteri-Staines, C.; Guerrero, J.M. Mitigation of Harmonics in Grid-Connected and Islanded Microgrids Via Virtual Admittances and Impedances. *IEEE Trans. Smart Grid* **2017**, *8*, 651–661. [CrossRef]
29. Isik, S.; Alharbi, M.; Bhattacharya, S. An Optimized Circulating Current Control Method Based on PR and PI Controller for MMC Applications. *IEEE Trans. Ind. Appl.* **2021**, *57*, 5074–5085. [CrossRef]
30. Ming, G.; Xiaohong, W.; Linping, W.; Daliang, W.; Weicheng, M.; Dong, Y. Research on Improved Circulation Suppression Strategy of MMC Based on Quasi-PR Controller. In Proceedings of the 2021 IEEE 5th Information Technology, Networking, Electronic and Automation Control Conference (ITNEC), Xi'an, China, 15–17 October 2021; pp. 106–109.
31. Ren, J.; Li, W.; Zhang, S. Study on AC Harmonic Characteristics of Netherland $\pm$525 kV/2 GW MMC-HVDC System for Offshore Wind Farms Integration. In Proceedings of the 2021 International Conference on Power System Technology (POWERCON), Haikou, China, 8–9 December 2021; pp. 1534–1541.